PHOTOELECTROCHEMICAL WATER OXIDATION ON HEMATITE FILMS IN NEUTRAL AND ALKALINE ELECTROLYTES

E. VASILE[a], M. SIMA[b,*], A. SIMA[c]
[a]*University "Politehnica"of Bucharest, Faculty of Applied Chemistry and Material Science, Department of Oxide Materials and Nanomaterials, No. 1-7 Gh. Polizu Street, 011061 Bucharest, Romania*
[b]*National Institute of Materials Physics, 405A Atomistilor Street, 077125 Magurele, Romania*
[c]*National Institute for Lasers, Plasma and Radiation Physics, 409 Atomistilor Street, P.O. Box MG-36 077125 Magurele, Romania*

Nanostructured hematite prepared via anodic deposition has been studied as photoanode in neutral and alkaline electrolytes. The morphology of the nanostructures was characterized by SEM, XRD analysis was performed to verify the phase of the films, absorption coefficient and band gap were determined from spectrophotometric measurements and the atomic concentration of Sn in hematite film was estimated from XPS measurements. EIS measurements and photocurrent responses showed the different behavior of hematite photoanode in alkaline and neutral electrolytes. The alkaline medium favors the chemisorption of the water molecules on hematite photoanode, contributing to the diminishing of the charge transfer resistance.

(Received April 4, 2020; Accepted July 22, 2020)

Keywords: Water oxidation, Hematite, Sn doped hematite, Electrolyte

1. Introduction

Conversion of solar energy into chemicals fuel through photocatalysis has gained a special interest [1-4] as a green and sustainable process for solving energy crisis and environmental pollution. Photoelectrochemical (PEC) and photocatalytic water splitting using semiconductors to generate hydrogen fuel is a part of this promising strategy. The water oxidation is the rate-limiting step of overall water splitting process due to the high activation barriers of oxygen generation. The most important properties of an efficient photocatalyst in oxygen generation [5-9] include a narrow band gap, a fast hole migration, a large surface area, a valence band maximum energy level more positive than the oxidation potential of water.

Hematite (α-Fe_2O_3) is a n-type semiconductor with a valence band edge position suitable for water oxidation and an optical bandgap of 2.1-2.2 eV [10-14]. It is stable in neutral and alkaline electrolytes. However, it is necessary to apply an external bias to generate hydrogen at counter electrode because its conduction band position is unfavorable for water reduction process [15, 16]. Like other semiconductors, hematite also has a short lifetime of minor carriers [12] and the kinetics for the transfer of holes at photoanode/electrolyte interface is slow [14]. The performance of state-of-art hematite photoanodes has been improved both by shifting of the onset potential towards more cathodic potentials and enhancing of photocurrent density [17]. The onset potential was shifted cathodically by two different paths: modification of photoanode surface with a co-catalyst, mainly cobalt-phosphate [18-21] to accelerate oxygen evolution reaction kinetics and depositing under or overlayers [22-26] of other semiconductors which lead to creating of homo or heterojonctions. The increasing of photocurrent density is typically achieved by material doping [27-31] and/or nanostructuring [14, 32-37].

* Corresponding author: msima@infim.ro

In the present study, the photoelectrochemical performance of simple and Sn doped porous hematite films was evaluated both in neutral and alkaline electrolytes in order to improve the water oxidation kinetics and the charge transfer process at photoanode/electrolyte interface.

2. Experimental

2.1. Samples preparation

Simple or nanostructured hematite films were prepared on FTO ($F:SnO_2$) substrate by an electrochemical method. FTO glasses (Solaronix, 7 ohm/square) were cleaned with detergent, water and acetone and sonicated with 2-propanole in an ultrasonic bath for 10 min. Thin films of hematite precursor (iron oxyhydroxide-FeOOH) were prepared on FTO substrate by electrodeposition in a conventional three-electrode cell that also contains a platinum foil as an auxiliary electrode and an Ag/AgCl electrode in saturated KCl as a reference electrode. The electrochemical process was performed potentiostatically at 1.2 V in a solution prepared by dissolving 0.1 M of $FeSO_4$ in the distilled water, using an Autolab PGSTAT 30 potentiostat. The hematite precursor was annealed at 525^0C resulting hematite film. In order to remove all hydroxyls from hematite it was necessary annealing over 800^0C. Nanostructured hematite film was prepared on FTO-hematite thin film substrate. A layer of agarose gel on substrate surface was used as template for electrodeposition of hematite precursor [38]. A 1% (w/v) solution of agarose powder was heated in distilled water in a microwave oven and the clear solution was cast on a substrate plate. The agarose solution forms a film on the substrate after three hours and a half at room temperature in a sealed container. Into the pores of the agarose gel is electrodeposited a nanostructured layer of FeOOH. The agarose template was removed by immersing the sample for one hour in water heated to 85^0C and the obtained porous film was annealed.

Sn-doped photoanode was prepared by dipping the hematite sample in an ethanol-$SnCl_4$ solution (5 mM) for 1 min. After dipping process, hematite sample was sintered at high temperature (800^0C for 10 min). The prepared samples are presented in the Table 1.

2.2. Structural and optical characterization

X-ray diffraction (XRD) analyses were performed on a Bruker D8 Advance type X-ray diffractometer, in focusing geometry, equipped with copper target X-ray tube and LynxEye one-dimensional detector. The microstructures of deposits were imaged by field emission scanning electron microscopy (FESEM), using FEY Quanta Inspect scanning electron microscopes.

The absorption spectra were recorded using UV-vis-NIR Carry 5000 spectrophotometer. X-ray photoelectron spectroscopy measurement was carried out on SPECS XPS spectrometer based on Phoibos 150 electron energy analyzer with non-monochromatic X-rays emitted by an anti-cathode of Mg (1253.6 eV). The electron energy analyzer was operated in constant energy mode with pass energy of 20 eV giving an energy resolution of 0.9 eV (FWHM of the Ag 3d5/2 line). The analysis chamber was maintained in ultra high vacuum conditions (~ 10^{-9} mbar). The C (1s) line (285 eV) corresponding to the C-C line bond had been used as reference Binding Energy (BE). The recorded XPS spectra were processed using Spectral Data Processor v 7.0 software.

2.3. Photoelectrochemical measurements

The photoelectrochemical measurements were carried out in 1 M NaOH (pH 13.6) and 0.5 M Na_2SO_4 (pH 7) electrolytes with a three-electrode electrochemical system composed of the FTO/hematite nanostructure as the working electrode, Ag/AgCl/saturated KCl as reference electrode, and a Pt foil as the counter electrode. The experimentally measured potentials vs. Ag/AgCl were reported against the reversible hydrogen electrode (RHE): $E_{RHE}=E_{Ag/AgCl}+0.059pH+E^0_{Ag/AgCl}$, with $E^0_{Ag/AgCl}=0.1976$ V at 25^0C. The working surface area of the hematite photoanodes was 1 cm^2. The photoanodes were illuminated from the front side (light falls on the semiconductor side) using AM1.5 solar simulator (L.O.T.-Oriel GmbH & Co.KG, Model LS0306 with a 300 W Xe-Arc lamp and an AM1.5-Global filter (LSZ189) with the specification: 1 sun at 18 cm working distance). The photocurrent-voltage (J-V) curves were measured in the dark and under illumination conditions with a scan rate of 20 mVs^{-1}. These measurements were conducted using a potentiostat/galvanostat Autolab PGSTAT 30 (Eco

Chemie). The electrochemical impedance spectroscopy (EIS) spectra were collected in a frequency range of 100 kHz to 0.1 Hz with amplitude of 10 mV. The obtained curves were fitted using a Zview software.

Table 1. The code of the hematite samples.

Hematite sample	Sample structure description	Deposition time (s)	Annealing step	Thickness (nm)
F1	FTO/hematite film	1000	525^0C, 2h	75
F2	FTO/hematite film/porous hematite	2200	525^0C, 2h; 800^0C, 10 min	215
F3	FTO-Sn doped hematite	2200	525^0C, 2h; 800^0C, 10 min	-

3. Results and discussion

3.1. Characterization of hematite films by XRD, SEM, UV-vis spectroscopy and XPS

The hematite film annealed at 800^0C (sample F2) exhibited typical diffraction peaks assigned to crystalline hematite ($2\theta=24.4^0$, 33.6^0; 35.9^0; 41.3^0; 49.6^0; 64.2^0 for (012), (104), (110), (113), (024) and (300) planes, respectively; see Fig.1a). The diffractogram of the sample F2 shows high intensity peaks which indicate high crystallinity of hematite film annealed at 800^0C.

Fig.1b shows SEM image of α-Fe_2O_3 film (F1) (Table 1) formed of small crystallites which derived from FeOOH film uniformly electrodeposited at 1.2 V for 1000s. Its thickness is of 75 nm (Fig. 1d). Fig.1c shows the porous morphology of nanostructured hematite sample (denoted F2) supplementary annealed at 800^0C and having a thickness of 215 nm. It consists of two layers, the porous layer being 140 nm thick (Fig. 1d).

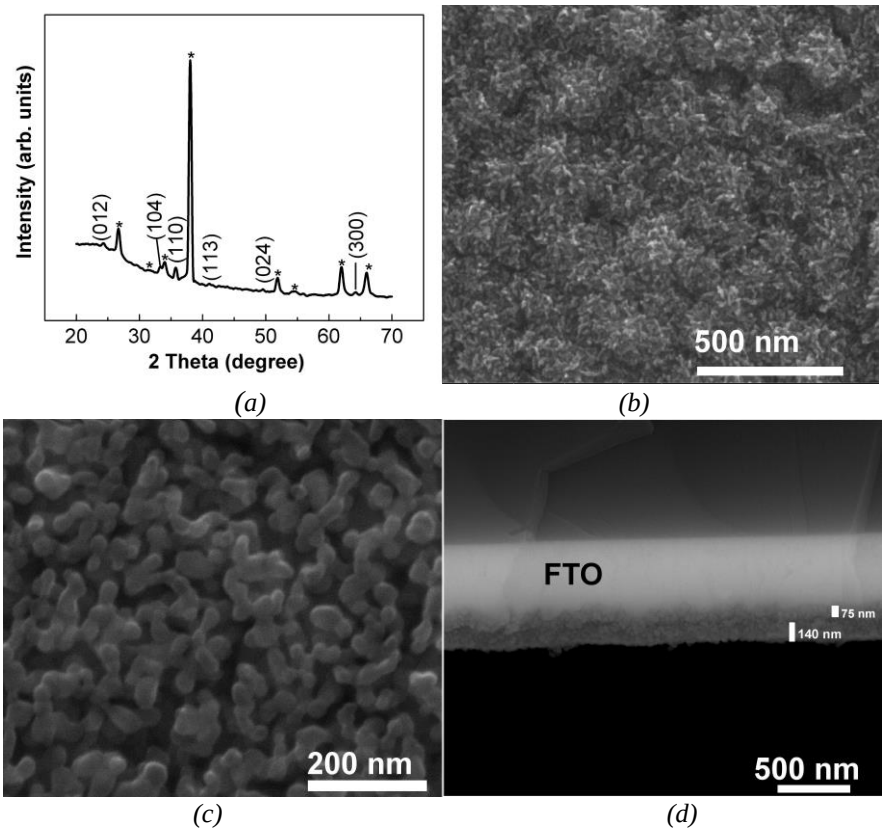

Fig.1. XRD pattern of the sample F2 (a) and SEM images of the samples F1 (b) and F2 (c and d).

Fig.2 shows UV-vis absorption spectra of the hematite samples F1, F2 and F3. Undoped hematite samples (F1 and F2) exhibit three absorption bands in visible spectrum at around 380 nm, 525 nm and 637 nm which are connected with a direct transition, an indirect transition and subband gap transitions, respectively. The direct transition corresponds to the O^{2-} 2p→ Fe^{3+} 3d charge transfer and indirect transition was identified as a spin-forbidden Fe^{3+} 3d→3d excitation [39].

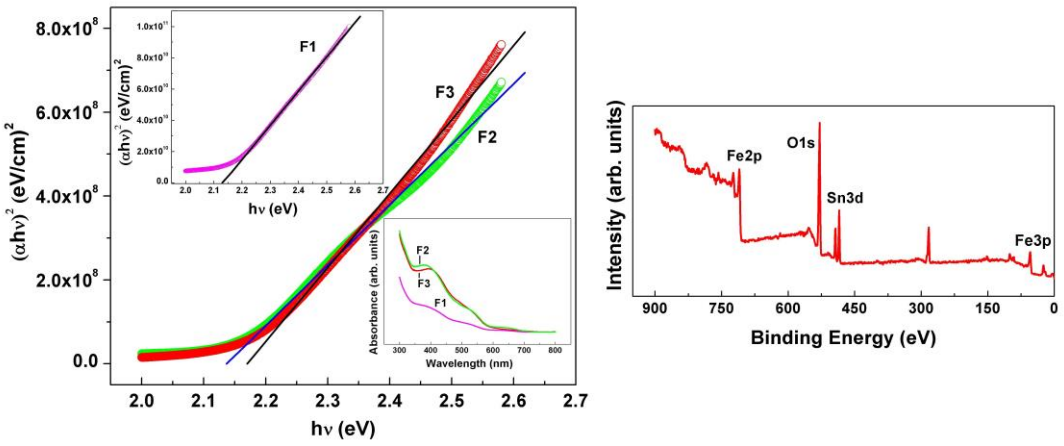

(a) *(b)*

Fig. 2. (a) Tauc plots of the samples F1 and F2; inset: UV-VIS spectra of the samples F1, F2 and F3; (b) XPS survey spectrum of the sample F3.

It can be observed that porous hematite film annealed at 800^0C shows an increased absorbance. The absorption band which corresponds to direct transition shows a red shift (at 393 nm) for Sn-doped hematite sample probable due to a distortion of the Fe_2O_3 lattice.

The optical bandgap energy (E_g) of the samples F1 and F2 was estimated using the following equation [40] and Tauc plot method [41]:

$$(\alpha h\nu)^n = B(h\nu - E_g) \quad (1)$$

where α is the absorption coefficient, hν is the photon energy, n equals 2 for a direct transition (direct band gap semiconductors) and B is a material-dependent constant. The absorption coefficient value was determined by following equation [42]:

$$\alpha = (-1/d)\ \ln (I_t/I_0) = (A/\log e) \approx 2.303A/d \quad (2)$$

where d is the sample thickness, I_0 and I_t are the intensities of incident and transmitted light, respectively, A=log (I_0/I_t) is the absorbance, obtained from the UV-vis absorption spectra. In order to obtain the band gap $(\alpha h\nu)^n$ was plotted as a function of photon energy (hν). The linear portions of the curves were fitted using linear regression analysis. An extrapolation of the linear regions of the plots gives the value of the bandgap as the intercept to x-axis (where αhν=0). The direct band gaps of the hematite samples F1 and F2 resulted from Tauc plots (Fig.2a) are very close (around 2.13 eV).

The XPS analysis was performed to confirm the presence of Sn dopant atoms after doping of hematite nanostructure. The XPS survey spectrum in Fig.2b depicted that sample F3 is constituted of Fe, O and Sn elements. The atomic concentrations of Sn and Fe were estimated to be 21.2% and 78.8%, respectively using Fe3p and Sn $3d_{5/2}$ peaks of XPS spectrum.

3.2. Photoelectrohemical characterization of hematite photoanodes

The performance of the prepared hematite photoanodes was evaluated from the photocurrent-voltage curves and electrochemical impedance spectroscopy measurements under simulated solar illumination (100 $mWcm^{-2}$) conditions.

Comparing the photoelectrochemical responses of the samples F2 an F3 it can be observed that sample F3 shows the highest photocurrent density at 1.23V vs RHE both in alkaline (1.08 mA/cm^2) and neutral (31 $\mu A/cm^2$) solution (Fig.3a and c). For the both samples, the photocurrents measured in alkaline solution are much higher. This larger value of the photocurrent obtained in alkaline solution could be attributed to changes in the characteristics of the photoanode surface which accelerate water oxidation kinetics and reduce interfacial recombination [43]. On the other hand, doping of hematite with Sn^{4+} ion produces a greather increase of the photocurrent in alkaline solution.

EIS data obtained under illumination conditions for the prepared photoanodes were interpreted with a model proposed by Klahr et al [43]. In this model the holes accumulate in surface states at the semiconductor/electrolyte interface. The process of water oxidation takes place mainly from these surface states.

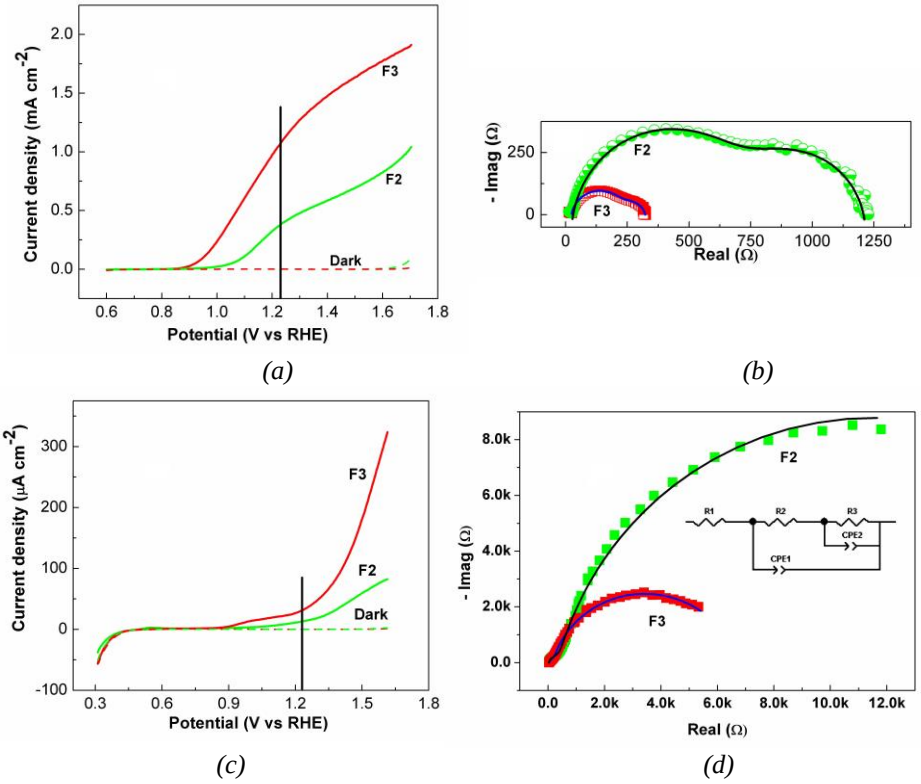

Fig. 3. J-V characteristics curves and EIS Nyquist plots at 1.23 V vs RHE obtained under simulated solar illumination of the samples F2 and F3 in alkaline (a and b) and neutral (c and d) solutions; inset: equivalent circuit for the simulation of photoelectrochemical mechanism in photoelectrodes.

Table 2. The parameters of the photoanodes obtained from impedance spectroscopy analysis.

	Alkaline electrolyte		Neutral electrolyte	
Photoanode →	F2	F3	F2	F3
R1 (Ωcm^2)	27.1	24.1	29.2	32.7
R2 (Ωcm^2)	771.9	221.1	558.7	493
R3 (Ωcm^2)	412.3	77.6	22093	6288
CPE1 (Fcm^{-2})	$9.1x10^{-6}$	$1.7x10^{-5}$	$1.5x10^{-5}$	$5.8x10^{-5}$
CPE2 (Fcm^{-2})	$2.1x10^{-4}$	$6.6x10^{-4}$	$5.1x10^{-5}$	$3.6x10^{-5}$

Fig. 3b and d show the Nyquist representations of the impedance spectra of the hematite photoanodes F2 and F3. These impedance spectra reveal two series charge transfer phenomena: charge trapping at surface states (arc at higher frequencies) and charge transfer from surface states to the aqueous electrolyte (arc at lower frequencies). The equivalent circuit used to fit the impedance data is also showed in the Fig. 3d. In this model, R1 represents resistance associated with the electrolyte resistance and electric contacts of the electrode, CPE1 is capacity associated with charge accumulation in the bulk, R2 is resistance in charge trapping process at surface states, the capacity CPE2 is correlated with the number of active centers from the surface states and R3 represents resistance in charge transfer process at photoanode-electrolyte interface.

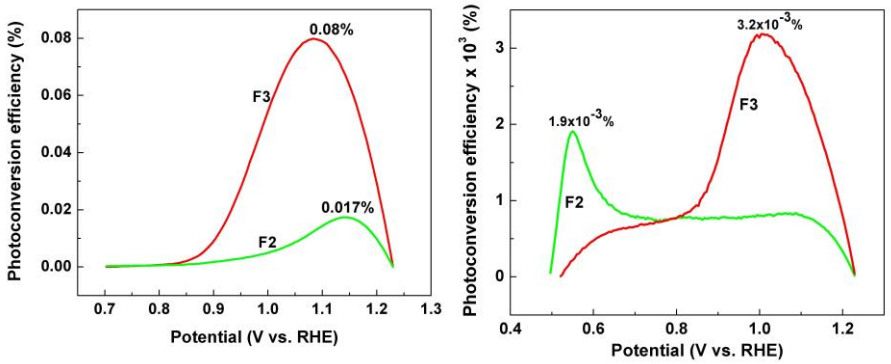

(a) *(b)*

Fig. 4. The photoconversion efficiency versus applied potential profile for samples F2 and F3 in alkaline (a) and neutral (b) solutions.

The oxygen evolution reaction involves four holes for each O_2 molecule. Based on the hypothesis that the holes are trapped by Fe species often referred as surface states (Fe-OH and Fe-O) from the hematite surface, it is observed (Table 2) that this process proceeds more easily in neutral medium ($R2_{neutral}<R2_{alkaline}$). However, the chemosorption of water molecules on these sites is obviously favored in an alkaline media ($R3_{alkaline}<<R3_{neutral}$). The presence of Sn^{4+} ions on the surface of the photoanode further activates the Fe species which reduces both R2 and R3 in both alkaline and neutral media. The obtained values of the CPE1 and CPE2 capacities are in accordance with the values of R2 and R3 resistances.

The applied bias photon-to-current efficiencies (ABPE, η) of these photoanodes for PEC water splitting were estimated. ABPE characteristics have been derived from the LSV plots from Fig.3a and c using equation 3 [44]:

$$\eta = \left(\frac{I*(1.23 - E_{app})}{P_{incident}}\right)*100\% \quad (3)$$

where I is photocurrent density (in $mAcm^{-2}$) under simulated sunlight, E_{app} the applied bias potential (V vs. RHE) and $P_{incident}$ is intensity of illumination light (100 $mWcm^{-2}$). The maximum efficiency values for F2 and F3 photoanodes in alkaline and neutral electrolytes are shown in Fig.4. It is observed that the value of maximum efficiency of Sn doped hematite (measured at 1.04 V/RHE) in alkaline solution is 25 times higher than its value in neutral solution. The values of maximum efficiency of the undoped hematite photoanodes are small, even in alkaline solution.

4. Conclusions

In summary, the photoelectrochemical properties of porous hematite based photoanodes have been studied both in alkaline and neutral electrolytes. The optical band gap of the hematite was 2.13 eV and the atomic concentrations of Sn and Fe in Sn doped hematite estimated from XPS measurements were 21.2% and 78.8%, respectively.

The photoanodes showed higher photocurrents in alkaline solution than in neutral solution. This could be attributed to changes in the characteristics of the photoanode surface which accelerate water oxidation kinetics and reduce interfacial recombination in alkaline electrolyte. Although the holes trapping by Fe species from the hematite surface proceed more easily in neutral medium, the chemosorption of water molecules on these sites is obviously favored in an alkaline media. Sn^{4+} ions on the surface of the photoanode further activate the Fe species. As a result, the values of the electrical resistances in charge trapping process and in charge transfer process at Sn doped hematite photoanode became smaller.

Acknowledgements

The financial support of Romanian Ministry of Education and Research (Core Program PN19-03, contract no. 21 N/08.02.2019) is gratefully acknowledged.

References

[1] A. G. Tamirat, J. Rick, A. A. Dubale, W.-N. Su, B.-J. Hwang, Nanoscale Horiz. **1**, 243 (2016).
[2] J. Mu, H. Miao, E. Liu, J. Feng, F. Teng, D. Zhang, Y. Kou, Y. Jin, J. Fan, X. Hu, Nanoscale **10**(25), 11881 (2018).
[3] J. H. Kou, C. H. Lu, J. Wang, Y. K. Chen, Z. Z. Xu, R. S. Varma, Chem. Rev. **117**(3), 1445 (2017).
[4] N. Fajrina, M. Tahir, Int. J. Hydrogen Energy **44**(2), 540 (2019).
[5] L. Mohapatra, K. Parida, J. Mater. Chem. A **4**(28), 10744 (2016).
[6] Z. Li, C. Kong, G. Lu, J. Phys. Chem. C **120**(1) 56 (2016).
[7] S. M. Thalluri, S. Hernández, S. Bensaid, G. Saracco, N. Russoa, Appl. Catal. B **180**, 630 (2016).
[8] F. Ning, M. Shao, S. Xu, Y. Fu, R. Zhang, M. Wei, D. G. Evans, X. Duan, **9**(8), 2633 (2016).
[9] S. Bai, X. Li, Q. Kong, Q. Long, C. Wang, J. Jiang, Y. Xiong, Adv. Mater. **27**(22), 3444 (2015).
[10] O. Zandi, A. R. Schon, H. Hajibabaei, T. W. Hamann, Chem. Mater. **28**(3), 765 (2016).
[11] H. Hajibabaei, A. R. Schon, T. W. Hamann, Chem. Mater. **29**(16), 6674 (2017).
[12] J. H. Kennedy, K. W. Fresse Jr., J. Electrochem. Soc. **125**(5), 709 (1978).
[13] M. P. Dare-Edwards, J. B. Goodenough, A. Hamnett, P. R. Trevellick, J. Chem. Soc., Faraday Trans. **79**(9), 2027 (1983).
[14] A. Kay, L. Cesar, M. Gratzel, J. Am. Chem. Soc. **128**(49), 15714 (2006).
[15] J. Cowan, C. J. Barnett, S. R. Pendlebury, M. Barroso, K. Sivula, M. Gratzel, J. R. Durrant, D. R. Klug, J. Am. Chem. Soc. **133**(4), 10134 (2011).
[16] M. Gratzel, Nature **414**, 338 (2001).
[17] B. Iandolo, B. Wickman, I. Zoric, A. Hellman, J. Mater. Chem. A **3**, 16896 (2015).
[18] M. W. Kanan, D. G. Nocera, Science **321**, 1072 (2008).
[19] D. K. Zhong, D. R. Gamelin, J. Am. Chem. Soc. **132**(12), 4202 (2010).
[20] D. K. Zhong, M. Cornuz, K. Sivula, M. Gratzel, D. R. Gamelin, Energy Environ. Sci. **4**(5), 1759 (2011).
[21] L. Halaoui, J. Phys. Chem. C **120**(40), 22766 (2016).
[22] T. Hisatomi, H. Dotan, M. Stefik, K. Sivula, A. Rothschild, M. Gratzel, N. Mathews, Adv.

Mater. **24**(20), 2699 (2012).
[23] L. Steier, I. Herraiz-Cardona, S. Gimenez, F. Fabregat-Santiago, J. Bisquert, S. D. Tilley, M. Gratzel, Adv. Funct. Mater. **24**(48), 7681 (2014).
[24] E. Vasile, M. Sima, A. Sima, C. Logofatu, Mater. Res. Bull. **121**, 0110623 (2020).
[25] M. Bartsch, M. Sarnowska, O. Krysiak, C. Willa, C. Huber, L. Pillatsch, S. Reinhard, M. Niederberger, ACS Omega **2**(8), 4531 (2017).
[26] D. Wang, X.-T. Zhang, P.-P. Sun, S. Lu, L.-L. Wang, Y.-A. Wei, Y.-C. Liu, Int. J. Hydrogen Energy **39**(28), 16212 (2014).
[27] Y. Liang,. C. S. Enache, R. van de Krol, Int. J. Photoenergy, 739864 (2008).
[28] A. Kleiman-Shwarsctein, Y.-S. Hu, A. J. Forman, G. D. Stucky, E. W. McFarland, J. Phys. Chem. C **112**(40), 15900 (2008).
[29] N. Mirbagheri, D. Wang, C. Peng, J. Wang, Q. Huang, C. Fan, E. E. Ferapontova, ACS Catal. **4**(6), 2006 (2014).
[30] S. Ida, K. Kearney, T. Futagami, H. Hagivara, T. Sakai, M. Watanabe, A. Rockett, T. Ishihara, Sustainable Energy Fuels **1**, 280 (2017).
[31] K. Sivula, F. LeFormal, M.Gratzel, ChemSusChem **4**(4), 432 (2011).
[32] R. Morrish, M. Rahman, J. M. D. MacElroy, C. A. Wolden, ChemSusChem **4**(4), 474 (2011).
[33] A. Mao, J.-G. Park, G. Y. Han, J. H. Park, Nanotechnology **22**(17), 175703 (2011).
[34] B. D. Chernomordik, H. B. Russell, U. Cvelbar, J. B. Jasinski, V. Kumar, T. Deutsch, M. K. Sunkara, Nanotechnology **23**(19), 194009 (2012).
[35] V. A. N. de Carvalho, R. A. D. Luz, B. H. Lima, F. N. Crespilho, E. R. Leite, F. L. Souza, J. Power Sources **205**, 525 (2012).
[36] L. Wang, C. Y. Lee, R. Kirchgeorg, N. Liu, K. Lee, S. Kment, Z. Hubicka, J. Krysa, J. Olejnicek, M. Cada, R. Zboril, P. Schmuki, Res. Chem. Intermed. **41**, 9333 (2015).
[37] L.-K. Tsui, Y. Xu, D. Dawidowski, D. Cafiso, G. Zangari, J. Mater. Chem. A **4**(48), 19070 (2016).
[38] M. Sima, E. Vasile, A. Sima, C. Logofatu, Electrochim. Acta **258**, 1453 (2017).
[39] A. Duret, M. Gratzel, J. Phys. Chem. B **109**(36), 17184 (2005).
[40] J. I. Pankove, Optical processes in semiconductors, Prentice-Hall, Englewood Cliff, NJ, 1971.
[41] J. Tauc, Amorphous and liquid semiconductors, Plenum, London, New York, 1974.
[42] A. D. Yoffe, Adv. Phys. **42**, 173 (1993).
[43] B. Klahr, S. Gimenez, F. Fabregat-Santiago, T. Hamann, J. Bisquert, J. Am. Chem. Soc. **134**(9), 4294 (2012).
[44] T. Hisatomi, J. Kubota, K. Domen, Chem. Soc. Rev. **43**(22), 7520 (2014).